DINAME 2023 - Proceedings of the XIX International Symposium on Dynamic Problems of Mechanics,
A.S. De Paula, A.T. Fabro and M.R. Machado (Editors), ABCM.
Pirenópolis, Go, Brazil, February 26th to March 3rd, 2023

Tie-rod Rotor Digital Twin Model - Theory & Experiment

Fernando Boeger Tezza[1], **Bruno Resende Ferreira Rende**[1], **and Ilmar Ferreira Santos**[1]

[1] Technical University of Denmark, Anker Engelunds Vej 101 2800, Kongens Lyngby - Denmark

Abstract:
This work aims to investigate the behavior of a tie-rod rotor taken from an industrial pump. In this system, the impellers and spacers are assembled in a modular fashion and are tightened using a nut at the end of the shaft. Three mathematical models with different assumptions are derived. In the first one, the shaft is considered as a conjunction of flexible elements and the impellers as rigid, while in the second the impeller flexibility is introduced;in the third the contact stiffness between the components is inserted into the model. The theoretical results are compared with experimental data using the first two bending modes for various pre-tensioning conditions. From the comparisons, it can be observed and quantified that one of the most important parameters influencing the system dynamics is the contact stiffness among rotor components (impellers).

Keywords: Tie-rod Rotor, Contact Stiffness, Experimental Modal Analysis, Digital-Twin, Pre-tensioning.

INTRODUCTION

It is well known that discs are essential components in rotating machines, for instance, in centrifugal compressors and pumps, they are the elements that transmit the kinetic energy from the rotating machine to the working fluid. One approach to assemble the discs in the shaft is to build a tie-rod rotor, in which a central bolt acts as the shaft, and discs are assembled in a modular fashion on the central bolt until fixed with a nut. The advantages of this procedure for rotors lie mainly in the straightforward modular aspect of the rotor parts and therefore a more effective assembly process. Differently from the integral rotors or non-tie-rotors, tie-rotors typically present nonlinear behavior, due to different parts being in contact with each other and, in extreme cases, rotor bolt self-loosening Li and Yuan (2020). The importance of the nonlinear aspects is determined by the contact status of interfaces that are influenced by the pre-loading conditions of the rotor and its external forces Gao et al. (2012). For instance, it has been reported in cases in which the contact interfaces create disparities in the natural frequencies in the order of 14%, Vannini (2014). Rimpel (2018) and Rimpel and Leopard (2019) proposed a curve fitting method combining experimental data and a finite element model. In the author's method, a very small element is created between the surfaces in contact and its modulus of elasticity is written as a function of the contact pressure using an empirical equation. The method showed good agreement with experimental tests. Gao et al. (2012) developed a mathematical model to represent the contact stiffness in rod-fastened rotors where both bending moment and tightening forces were considered. The results of a simplified rotor model indicated that, for a fixed pre-tightening force, the equivalent flexural stiffness of the contact layer decreases with bending moments in the first contact state, whereas it increases with bending moments in the second contact state. Oh, Kim, and Palazzolo (2021) combined the general contact theory model with a finite element model to represent the contact forces. In the author's work, the simulated results greatly matched the experimental data, highlighting the model reliability with regard to the interface surface roughness and the increase of pre-loads. All the aforementioned literature serves as foundation for the model presented in this work. The rotor to be modelled hereafter is taken from an industrial pump, which is considered a tie-rod rotor type. The rotor model consists of a shaft assembled to 12 closed-type impellers, separated by 11 similar spacers and fastened by two Belleville washers and one nut (Figure 1). To study the dynamics of the system, three different approaches are considered. The first approach will follow Nelson and McVaugh (1976), in which the rotor is modeled as a flexible element and the impellers are considered rigid, thus contributing only with mass and inertia. In the second approach, the impellers and the shaft are treated as flexible as the calculations are done in a commercial finite element program – ANSYS. Finally, in the third approach the rotor and the impellers are modelled as flexible elements and the contact stiffness between the impellers and spacers is inserted into the model. The contact stiffness is calculated based on Greenwood and Williamson (1966). The outcomes of the three models are then compared with results obtained from an experimental modal analysis of the rotor in

a non-spinning free-free condition. During the experiments, different tightening forces are applied in the rotor, aiming at investigating the influence of this force on the system dynamics. The accuracy of the three modeling approaches, followed by their advantages and limitations, are the main outcomes of this analysis.

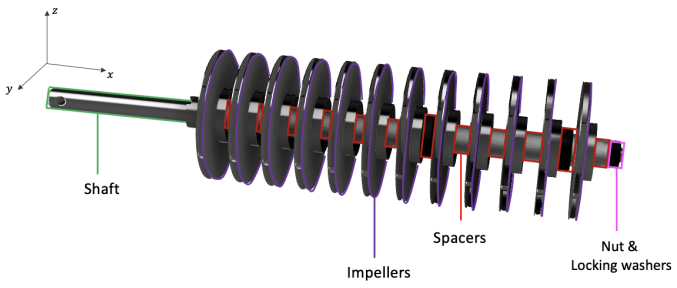

Figure 1 – Tie-rod rotor from an industrial water pump.

MATHEMATICAL AND SIMULATION MODELS

Model with Flexible Shaft and Rigid Impellers

The first model studied in this work considers the rotor as a flexible beam, the displacements of which are discretized using finite elements, and the impellers and spacers as point masses; thus contributing only with mass and inertia. Figure 2 shows how the shaft is discretized in 37 elements.

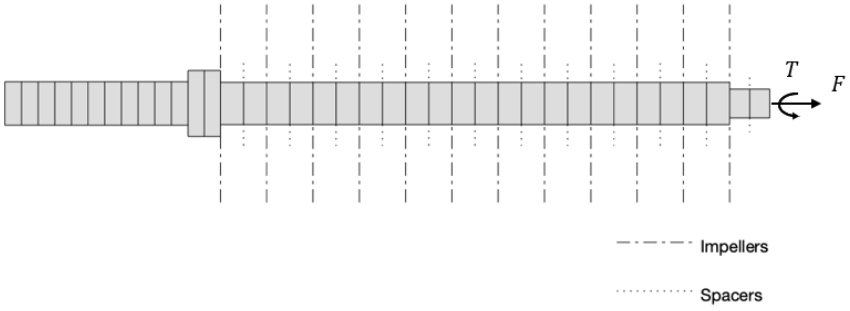

Figure 2 – Shaft FE Discretisation Model, F being the axial force generated by the torque T.

All the elements of the shaft have four degrees of freedom per node (two translations and two rotations) and the shear effect was neglected, as the length of the rotor is significantly larger than its diameter. The nut tightening effect is included in the model with the following matrix obtained from Nelson and McVaugh (1976):

$$\mathbf{K_F}^e = \frac{F}{30l}\begin{bmatrix} 36 & & & & & & & \\ 0 & 36 & & & & & & \\ 0 & 3l & 4l^2 & & & \text{sym} & & \\ -3l & 0 & 0 & 4l^2 & & & & \\ -36 & 0 & 0 & 3l & 36 & & & \\ 0 & -36 & -3l & 0 & 0 & 36 & & \\ 0 & 3l & -l^2 & 0 & 0 & -3l & 4l^2 & \\ -3l & 0 & 0 & -l^2 & 3l & 0 & 0 & 4l^2 \end{bmatrix}, \tag{1}$$

being, l the element size and F the axial loading force.

Thus, the dynamic equation for the rotor system can br written as:

$$\underbrace{(\mathbf{M_T^r}+\mathbf{M_R^r})}_{\mathbf{M^r}}\cdot\ddot{\mathrm{q}}^{\mathrm{r}}-\Omega\cdot\mathbf{G^r}\cdot\dot{\mathrm{q}}^{\mathrm{r}}+\underbrace{(\mathbf{K_B^r}+\mathbf{K_F^r})}_{\mathbf{K^r}}\cdot\mathrm{q}^{\mathrm{r}}=\mathrm{Q}^{\mathrm{r}}, \tag{2}$$

being $\mathbf{M_T^r}$ and $\mathbf{M_R^r}$ the translational and rotational mass matrices, $\mathbf{G^r}$ the gyroscopic matrix, and $\mathbf{K_B^r}$ and $\mathbf{K_F^r}$ the structural and axial load stiffness matrices. The mass and stiffness matrices are extracted from Nelson and McVaugh (1976). It is important to emphasize that, in this study the rotor was kept at rest, $\Omega = 0$ and no external loads were applied in the system, $\mathrm{Q}^{\mathrm{r}} = 0$.

Model with Flexible Shaft and Flexible Impellers

Aiming at including the impeller flexibility, a second model is built aided by ANSYS. Hence, the whole system was discretized using elements of type SOLID 187 with an element size of 2 *mm*. Figure 3 illustrates the whole procedure in detail: 1) placing a fixed boundary condition (BC) at the position of the first impeller and defining a force load case; 2) contact stiffness definition among all the parts; 3) solving the model in a Static Structural condition; 4) updating the system structural stiffness matrix with the Static Structural results; 5) removing the fixed Static Structural BCs and 6) executing a *free-free* Modal Analysis.

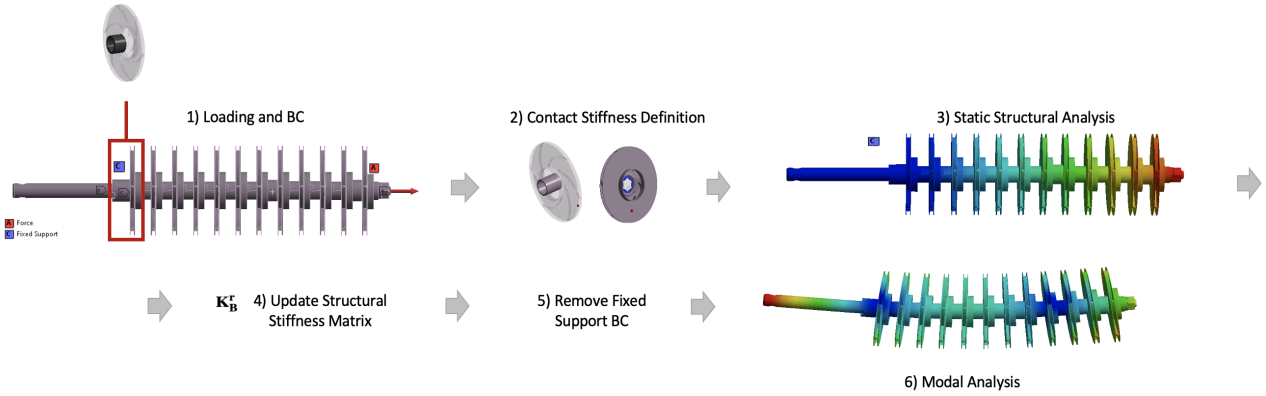

Figure 3 – ANSYS pre-loading simulation model - steps from the modeling until the static and dynamic analyses.

As can be seen from the description of the modeling procedure, the loading condition is set up in step 1) assuming that the shaft elongates while the impellers move along with no axial constraints. Nevertheless, in reality, when torque is applied to the rotor, all the impellers and spacers are set in compression as the shaft is tensioned.

Contact Stiffness Modelling

When considering contact surfaces, it is obvious that the real and nominal areas may differ from one another due to the existence of asperities. It should be noted that the differences between the real and nominal contact areas affect the analysis of the contacting regions. Therefore, the shapes of the contacting areas should be determined. According to Williams (1994), in the Hertzian contact theory, the contacting bodies are considered to be smooth, frictionless and elastic, meaning a non-adhesive contact where no tension force is allowed to occur within the contact area.

Thus, trying to expand Hertz's theory in a more detailed model, Greenwood and Williamson (1966) developed a method for elastic contact between nominally flat surfaces, known as the GW method. This method, considers that elastic contact occurs between a plane and a nominally flat surface with different asperities. It is also accounted that the summits of the asperities are almost spherical and the radii of asperity summits are assumed to be the same all over the surface. The model also considers a Gaussian asperity with a perfectly symmetric surface height distribution. From the model it is possible to define the contacting asperity pressure, P_C and the total contact area at the asperities, A_C:

$$P_C(h) = \frac{4}{3}\eta\beta_s^{\frac{1}{2}}\sigma_s^{\frac{3}{2}}E'F_{\frac{3}{2}}(h); \quad A_C(h) = \pi\eta\mathrm{A}_0\beta_s\sigma_s F_1(h) \tag{3}$$

where, $\sigma_s = \sqrt{\sigma_{s1}^2 + \sigma_{s2}^2}$ is the combined asperity summits height standard deviation (m), $\beta_s = \sqrt{\frac{\beta_{s1}^2 \beta_{s2}^2}{\beta_{s1}^2 + \beta_{s2}^2}}$ is the combined asperity summits mean radius (m), $\eta = \sqrt{\eta_1^2 + \eta_2^2}$, the combined asperity summits density (m^{-2}), A_0 is the nominal contact area (m^2), $F_n(h)$ is the integral of summit height distribution, $E' = \frac{E_1 E_2}{E_1(1-\nu_2^2)+E_2(1-\nu_1^2)}$ is the two-surfaces elastic modulus (Pa), d is the separation between the two surfaces (m) and h is the standardized separation, given by $h = \frac{d}{\sigma_s}$. All the indexes for the combined surfaces in which $i = 1,2$ in σ_{si}, β_{si}, η_i, E_i and ν_i are given for surfaces 1 and 2, Tomanik et al. (2021).

The integral of summit height distribution is derived as below:

$$F_n(h) = \int_h^\infty (s-h)^n (1/\sqrt{2\pi}) e^{-\frac{s^2}{2}} ds, \tag{4}$$

in which the summit height distribution is considered following a normalized Gaussian distribution.

Furthermore, in a similar manner, for the contact stiffness Thomas and Sayles (1977) developed a method based on GW assuming that the surface is loaded elastically against a plane over a nominal area A_0, in which the standardized separation h of their mean planes is related to a load P_C, as:

$$k_N(h) = \frac{4}{3} \eta \beta_s^{\frac{1}{2}} \sigma_s^{\frac{1}{2}} E' F_{\frac{1}{2}}(h), \tag{5}$$

Above, the terminology summit has been mentioned for defining different variables. Figure 4 shows the difference between the summit and roughness distributions.

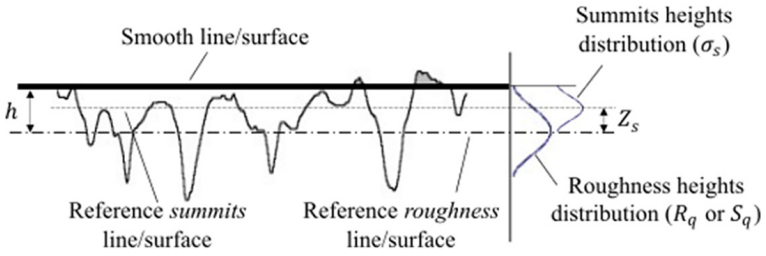

Figure 4 – Statistical distributions of the roughness and summits heights, Tomanik et al. (2021).

To easily understand this difference, it is valid to mention that the Reference roughness line/surface indicates the point in which all the heights are equal to zero. Therefore, all above the Reference roughness line/surface indicates positive heights, meaning that this region is the only part of the roughness profile that may touch another surface.

Conclusively, using Equation 5 and going back to Figure 3, specifically to point 2), it is now possible to define the afore missing contact stiffness. On the other hand, however, using Equation 5, it is possible to see that k_N is a function of η, $F_n(h)$, β_s, σ_s and h, all obtained with experimental data. In the same way, the force used to generate the torque applied at the rotor nut also needs an experimental setup for its acquisition. Fostering this data collection, the next parts expands on all the experimental set-ups necessary for collecting data and hence solving/validating the models so far presented.

EXPERIMENTAL FACILITY

Static Force Measurements

To evaluate the mathematical models presented, experiments were carried out. The setup used is illustrated in Figure 6, where the rotor is hung by wires in a free-free condition and an electromagnetic shaker (model 4809 Brüel & Kjær), c.f.#3, is attached to its tip to excite the system. On the left side of this figure, one can note the accelerometer (type 4393

Brüel & Kjær), c.f.#2, the dynamic force transducer (type 8200 Brüel & Kjær), c.f.#1, used, respectively, for measuring the acceleration of the shaft and the force applied by the shaker. While on the right side, the washer force transducer (Brüel & Kjær, model KMR with a capacity of 60 kN), c.f.#4, is placed after the nut to measure the tightening force. The data is recorded using a dSpace controller board type CP1104, using a sampling rate of 6 kHz. It is very important to add that the accelerometer and the force transducer that measure the dynamic force were connected to a charge amplifier, Brüel Kjær model 2635, which is set to filter the signals using an analog low-pass filter with a cut-off frequency of 3 kHz to avoid aliasing.

The experiments are conducted for torques varying from 1 to 15 $N.m$ and are repeated four times for the same torque. A chirp signal is sent to the shaker to excite the system in the frequency range from $0-1500$ Hz. Figure 6 shows the force average results accompanied by its sample standard deviation (68%). As for the force, the sample standard deviation curves show that the measures indeed have some uncertainty that seem to vary linearly within an interval and then stabilize. In a general perspective, it is difficult to precisely point out why this stabilization appears for higher torques. However, it must be highlighted that the force transducer is over dimensioned for the application, since it is rated for 60 kN, while the maximum force applied is approximately 2.5 kN.

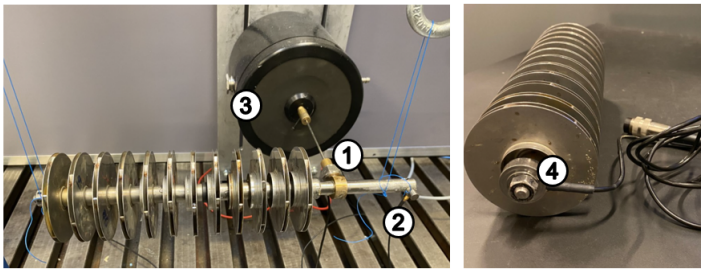

Figure 5 – Experimental setup

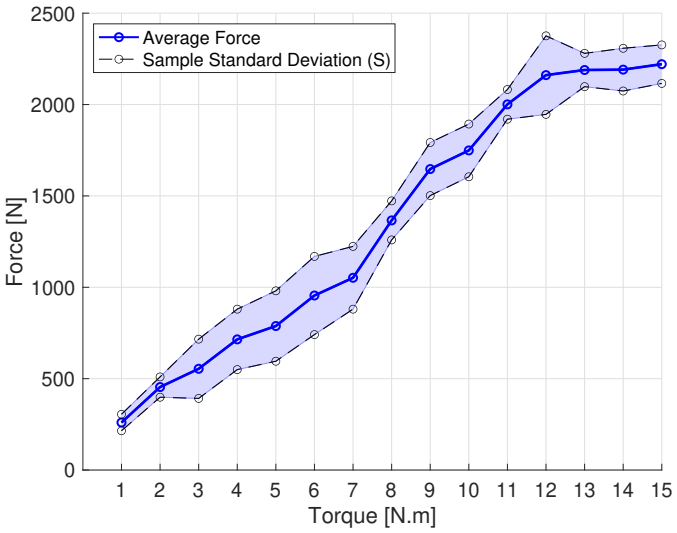

Figure 6 – Torque versus Average Force and Sample Standard Deviation.

Surface Roughness Parameters Measurements

For obtaining the contact stiffness among the rotor component contacts, the equipment Alicona Infinite Focus is used, Figure 7. The main component of the machine is a precision optic containing various lens systems that can be equipped with different objectives allowing measurements with different resolution. For executing the experiment, it is planned to measure all the contact areas presented in Figure 8 a), with that, Figure 8 b) shows all the parts that have been selected for

the measurements.

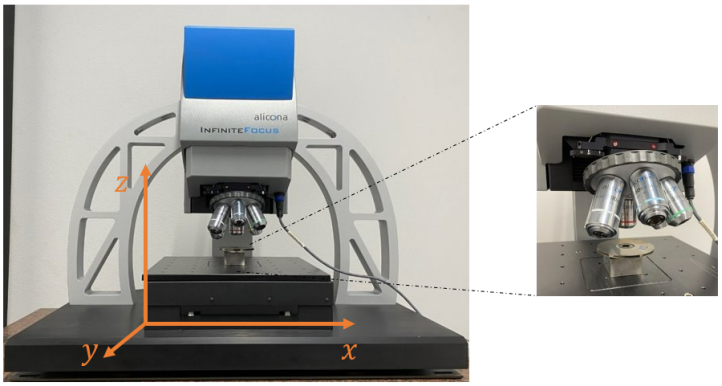

Figure 7 – Alicona Infinite Focus and detailed view of the impeller and lenses.

The summit roughness parameters can be calculated as:

$$\sigma_s = \sqrt{\frac{1}{L}\int_0^L z_s{}^2\,dx}; \quad \eta = \left(\frac{n_p}{L}\right)^2; \quad \beta_s = \sum_0^{n_p}\left(\frac{x(p_{n_p+1}) - x(p_{n_p})}{2}\right)\frac{1}{n_p} \tag{6}$$

being, L the profile length, z_s the summit profile roughness, n_p the number of peaks, x the position of a peak, p_{n_p+1} the location of a point from a peak position shifted 4 positions in the positive direction of x and p_{n_p-1} the location of a point from a peak position shifted 4 positions in the negative direction of x. It is valid to mention that β_s is here written as the average radii in each profile.

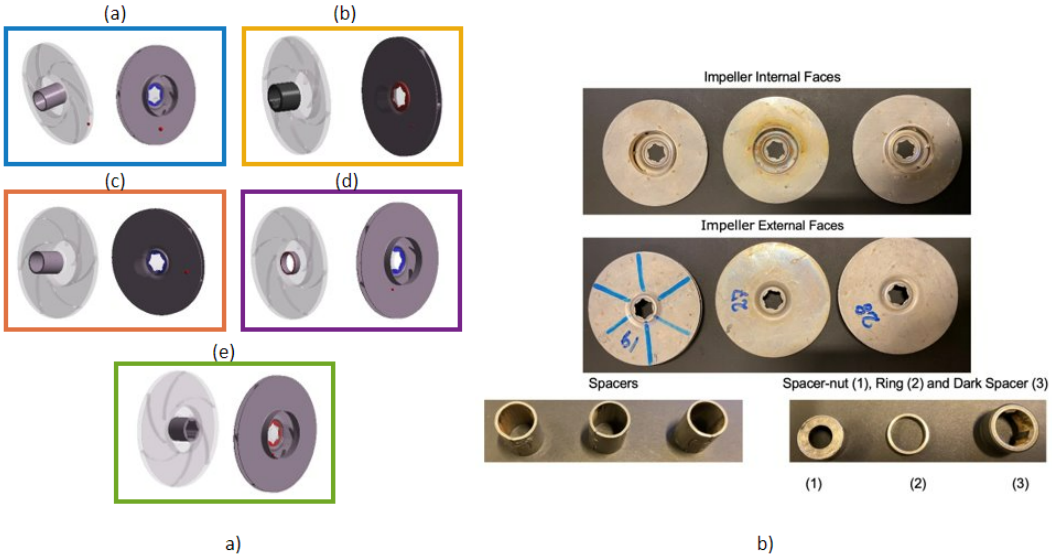

Figure 8 – a) Contact areas: (a) Spacer - Internal Impeller, (b) Dark-Spacer - External Impeller, (c) Spacer - External Impeller, (d) Ring - Internal Spacer and (e) Spacer-nut - Internal Impeller & b) Parts selected for being measured by the Alicona, in total: 3 Impellers, 3 Spacers, 1 Spacer-nut, 1 set Dark-Spacer and Ring. For all the specific component names, c.f # Figure 8 b).

The results of the roughness parameters averages for the impellers and spacers can be found in Tables 1 and 2, S_{EF} and S_{IF} being the one sample standard deviations of the external and internal impeller faces, respectively. From the results, it is reasonable to comment that both the external and internal face results are in the same order of magnitude presenting a low standard deviation. Lastly, still regarding the tables, the average Kurtosis of the measurements ($\overline{K}_u$) is presented. As

shown, the average of the measurements is over 3, meaning a non-Gaussian distribution; nevertheless it should be noted that the one sample standard deviation is great (more than 10% of the original value) for both sides of the impellers, which may reflect errors intrinsic to the measurements (e.g: corrosion or impurities on the surface).

Table 1 – Average values and sample standard deviations for the impeller roughness parameters.

	External Face	Internal Face	S_{EF}	S_{IF}
$\overline{\sigma_s}$ $(\times 10^{-6})$ $[m]$	0.7101	0.4220	2.5466×10^{-8}	1.7343×10^{-8}
$\overline{\beta_s}$ $(\times 10^{-4})$ $[m]$	0.1401	0.2581	4.8165×10^{-7}	3.0585×10^{-7}
$\overline{\eta}$ $(\times 10^{8})$ $[m^{-2}]$	1.7563	1.2972	3.0026×10^{7}	1.6982×10^{7}
$\overline{K_u}$	3.7682	3.9201	0.4780	0.9776

Table 2 – Average values and sample standard deviations for the spacers roughness parameters.

	Face and Bottom	S_{FB}	Dark-Spacer Face	Ring Face	Spacer-Nut Face
$\overline{\sigma_s}$ $(\times 10^{-6})$ $[m]$	0.2427	0.9493×10^{-7}	0.3391	0.3097	0.4933
$\overline{\beta_s}$ $(\times 10^{-4})$ $[m]$	0.1201	0.28892×10^{-7}	0.2519	0.2261	0.1831
$\overline{\eta}$ $(\times 10^{8})$ $[m^{-2}]$	3.2831	1.2842×10^{8}	1.7516	2.4368	3.1061
$\overline{K_u}$	3.3098	0.3472	3.7130	2.7337	3.8931

The average experimental values presented in Tables 1 and 2 can be applied to Equations 3 and 5 for calculating the contact pressure and stiffness; however, one assumption is still remaining. As shown, both equations are dependable on the separation between the two surfaces. In reality, this separation will not be measured and needs to be either defined by some model or overcome by an assumption. Figure 9 shows a flowchart with the procedure used for solving Equations 3 and 5 due to the assumption that $\left|\frac{P_C(h)-P_{C,comp}}{P_{C,comp}}\right| < tol$, being $P_{C,comp} = \frac{F}{A_{comp}}$, in which $P_{C,comp}$ is the contact pressure on the component contact (e.g.: spacer - impellers), F is the experimental force measured (Figure 6), A_{comp} is the nominal area of contact in between the two different components and tol is the tolerance set to 1%.

The first step in the flowchart is to initialize the variables for each surface. Having the initial variables calculated, the next step is to assume a distance, d, which the two surfaces can potentially have. In this case a range of $d = [10^{-8}, 10^{-6}]$ m is defined. With these distances, a loop can be executed for defining the output vectors of P_C and k_N all in function of h. Lastly, another assumption is made for comparing the pressure at the contact, P_C, with the nominal pressure in regards of the area created with each of the components, $P_{C,comp}$, leading to $P_{C,comp} = P_C$. Due to this assumption it is now possible to search for values of $P_{C,comp}$ that are equal to P_C, meaning that a vector h^* of dimensionless separation smaller in size than h, can be tracked. With h^* obtained, the contact stiffness can be finally derived as $k_N(h^*)$. It is valid to highlight that the assumption of $P_{C,comp} = P_C$ stands on the fact that the contact area of the components is A_0. Verily, this assumption is contrary to what the GW model postulates since $A_C < A_0$ (see Equation 3). In reality, finding the real area of the contact also depends on finding the dimensionless separation h between the two surfaces. As this separation is not measured in this work, one of the subterfuges used is to consider $P_{C,comp} = P_C$. Physically, this means that all the possible asperities in the contact region are touching each other and that finding one h for each of the contact pressures P_C is equivalent to regulating a theoretical distance that would generate the same contact pressure and stiffness results. The execution of the algorithm yields to the contact stiffness for all the aforementioned contact areas, Figure 10.

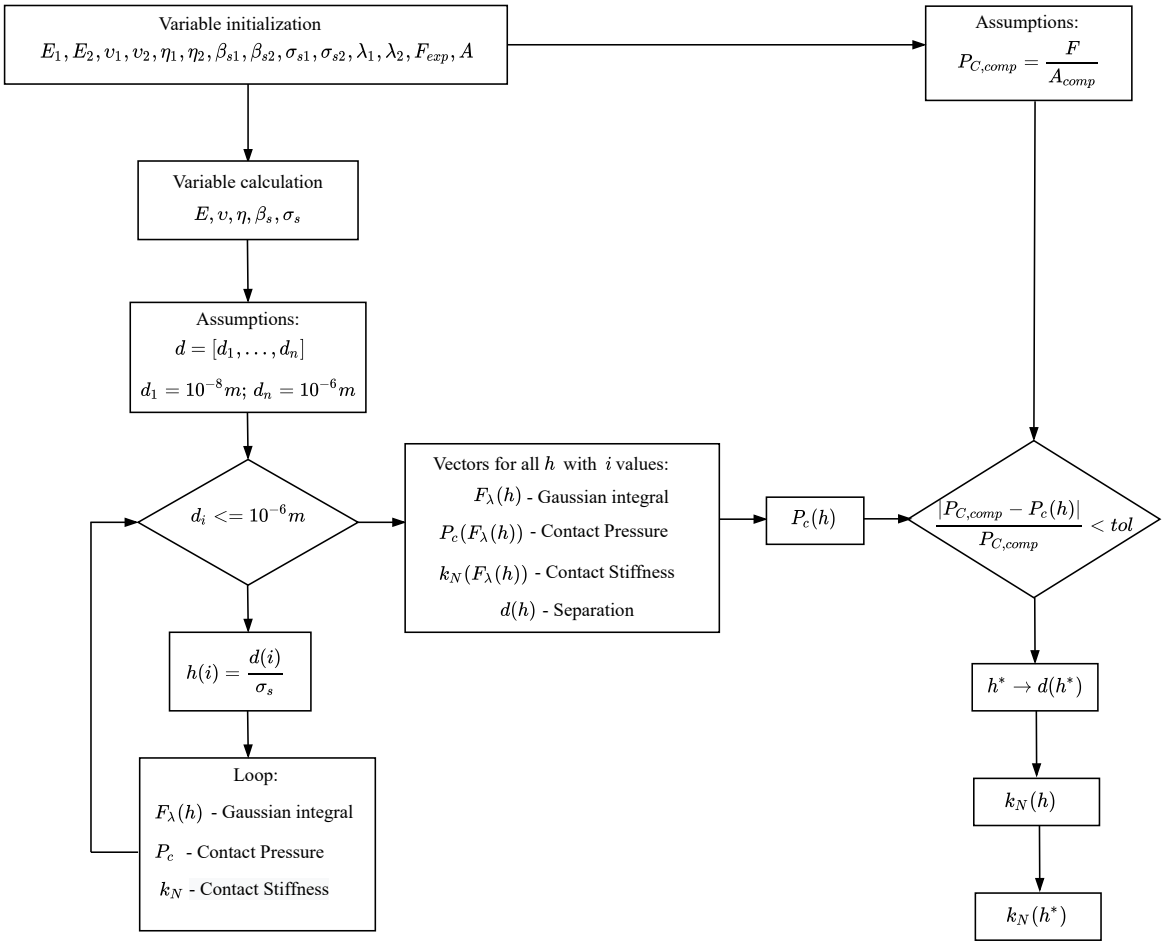

Figure 9 – Contact Pressure and Stiffness calculation algorithm flowchart.

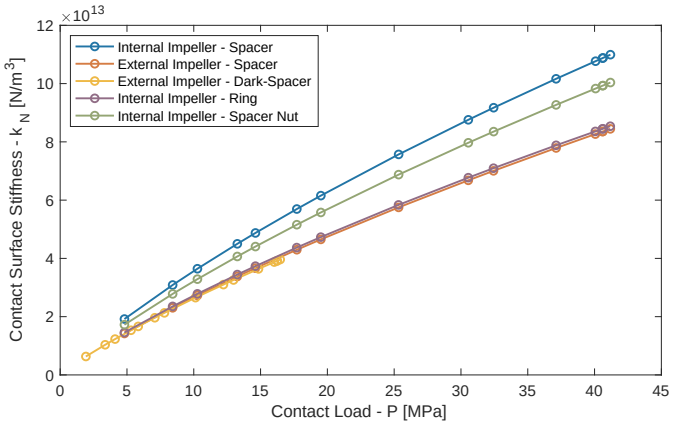

Figure 10 – Contact stiffness curves for all the different contacting components coloured according to the contact areas of Figure 8 a).

From Figure 10, it is possible to see that the contact stiffness values of all the curves tend to increase in a polynomial form with the contact pressure. By comparing the curves among themselves, it is possible to see that there is either an impact in the values due to the contact area, the roughness parameters or the superposition of both. For instance, while comparing the blue and orange curve, it can be inferred that both contact areas are the same, thus directing the main cause of difference to the roughness parameters. Following the same comparison reasoning, the blue and purple curve present different areas and roughness parameters, meaning that potentially the impact in the values can be harnessed to the superposition of both effects. As a note, it shall be highlighted that the External Impeller - Dark Spacer curve (yellow) has much lower pressure values than all the other contact zones given that the contact area of these components is much larger than the others.

EXPERIMENTAL RESULTS AND MODEL VALIDATION

In this section, the natural frequencies calculated using the three different models are compared with experimental results. For the mathematical models the natural frequencies are obtained by solving the eigenvalue problem, while the experimental natural frequencies are estimated by finding which frequencies corresponded to the peaks in the amplitude of the frequency response function. The comparison is illustrated on the left side of Figure 11. In pairs, the blue (- - ⊖ - -) and red (- - ⊖ - -) dashed lines with circle data points represent the natural frequencies estimated experimentally. On the other hand, to calculate the theoretical frequencies, one needs to have knowledge about the tightening force applied on the rotor. This force is obtained experimentally, c.f. # Figure 6, and is introduced in the mathematical model. The frequencies calculated by the first model, in which the impellers are considered rigid and the contact stiffness is neglected, are depicted by the dashed lines with diamond data points (- - ◇ - -). Similarly, the dashed lines with asterisk data points (- - ✳ - -) show the results obtained by the model for the same rotor flexible shaft, but now coupled to flexible impellers and still without any contact stiffness. The blue (- - △ - -) and red (- - △ - -) dashed lines with triangle data points outline the rotor dynamics coupling impeller flexibility and contact stiffness. From the experimental data – (- - ⊖ - -), (- - ⊖ - -) – and mathematical modelling – (- - ◇ - -) – frequency result comparisons, it can be seen that the mathematical model can fairly predict the first rotor bending mode for low values of torque. Contrary to this fact, when the torque increases the difference in between the curves also seems to increase. Analogously, for the second mode these differences seem to be even larger than for the first mode. All of these differences are numerically quantified and presented at the right of Figure 11, by the relative deviations for the first and second bending mode, $\Delta\omega_1$ and $\Delta\omega_2$, respectively. In an overall representation, the model with rigid impellers seems not to cover the overall rotor dynamics.

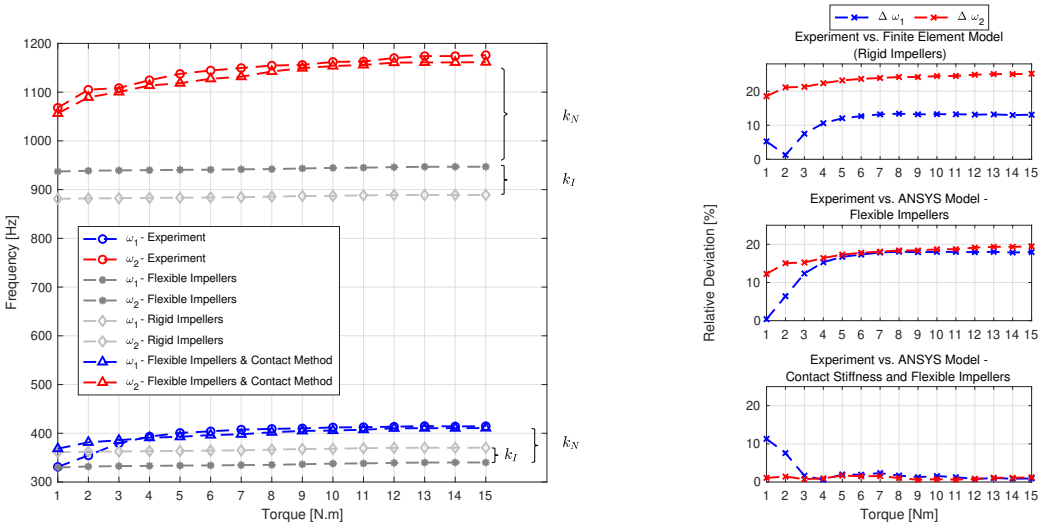

Figure 11 – Left: Impeller flexibility and contact stiffness natural frequency influence for the rotor in a pre-loading condition, in which k_N and k_I are the contact and impellers stiffness. Right: Relative deviations of the experimental data compared to the simulated results.

For highlighting the impeller flexibility influence, a direct comparison between the systems having the flexible and rigid impeller, i.e., – (- - ◇ - -) and (- - ✳ - -), is made. For such, this comparison lies in the fact that the two systems differ solely in having the addition of the impeller flexibility (k_I). Graphically, this inclusion depicts the phenomenon of having the first and second bending modes decreasing and increasing the system natural frequencies, respectively relatively to each other. By the relative deviations, Figure 11 right side second graph, it can be commented that the addition of the impeller flexibility slightly improves the model for the second bending mode, but does the contrary for the first. Going back to Figure 11 left side, but now looking at systems having the flexible impellers and both the flexible impellers and contact stiffness –(- - ✳ - -) and (- - △ - -), (- - △ - -), it can be noticed that there is a larger shift of both modes given the introduction of the contact stiffness (k_N). As portrayed in the figure, the contact stiffness inclusion not only provides the major influence in the model results for both modes when compared to the simulated data, but also makes the simulation results nonlinear.

Finally, focusing on the experimental – (- - ⊖ - -), (- - ⊖ - -) – and simulated results when the contact stiffness is

included in the model – (- - △ - -), (- - △ - -) – it can be seen that both the simulated and experimental results quite agree with each other, less than 5% deviation for most loading conditions (Figure 11 right side third graph). Nonetheless, special attention shall be taken to the first bending mode for torques lower than 3 $N.m$. Reasoning on this point, it can be articulated that these deviations can potentially have occurred because the simulations do not take in consideration the contact slips. In fact, this phenomenon is explained by the verity that the nonlinear behaviour of joints create signal dependent FRF's, meaning that the energy increment in the force signal may be dissipated by the joint friction yielding decreasing modes, Ewins (2009).

CONCLUSION

This work aimed to evaluate three different models of a tie-rod rotor: The first following the traditional approach used in rotordynamics, the second considered the impellers as flexible bodies, and the third the flexibility of the impellers and the contact stiffness among the components. The rigid impeller case depicts the largest difference in natural frequencies when compared to the experimental data, more than 10% and 20% deviation for the first and second bending modes, respectively for most of the loading cases. By the same reasoning, when considering the simulations with flexible impellers, it is well-known that discrepancies are mostly under 20% deviation for both the second and first bending modes. However, by comparing these results with the previous model, it can be commented that the inclusion of the impeller flexibility does not seem to improve the model result convergence to the experimental data. By including the contact stiffness on the flexible impellers model the discrepancies between the theoretical and experimental results are strongly reduced, less than 5% for both modes and most loading cases. Therefore, this result shows that not only is the impellers flexibility important to accurately describe the lateral dynamics of the rotor assembly, but largely also the contact stiffness among the different components.

REFERENCES

Li, Pu and Qi Yuan (2020). "Determination of contact stiffness and damping of a tie-bolt rotor with interference fits using model updating with thin-layer elements". In: *Shock and Vibration* 2020.

Gao, Jin et al. (2012). "Effects of bending moments and pretightening forces on the flexural stiffness of contact interfaces in rod-fastened rotors". In: *Journal of Engineering for Gas Turbines and Power* 134(10).

Vannini, Giuseppe (2014). "Rotordynamic validation of an ultra high speed multistage centrifugal compressor stacked rotor". In: *Turbo Expo: Power for Land, Sea, and Air*. Vol. 45769. American Society of Mechanical Engineers, V07AT31A038.

Rimpel, Aaron M (2018). "A simple contact model for simulating tie bolt rotor butt joints with and without pilot fits". In: *Turbo Expo: Power for Land, Sea, and Air*. Vol. 51135. American Society of Mechanical Engineers, V07AT33A003.

Rimpel, Aaron M and Matthew Leopard (2019). "Simple contact stiffness model validation for tie bolt rotor design with butt joints and pilot fits". In: *Turbo Expo: Power for Land, Sea, and Air*. Vol. 58684. American Society of Mechanical Engineers, V07AT33A005.

Oh, Joseph, Baik Jin Kim, and Alan Palazzolo (2021). "Three-dimensional solid finite element contact model for rotordynamic analysis: Experiment and simulation". In: *Journal of Vibration and Acoustics* 143(3).

Nelson, HD and JM McVaugh (1976). "The dynamics of rotor-bearing systems using finite elements". In.

Greenwood, James A and JB Pl Williamson (1966). "Contact of nominally flat surfaces". In: *Proceedings of the royal society of London. Series A. Mathematical and physical sciences* 295(1442), pp. 300–319.

Williams, JA (1994). "Engineering tribology Oxford University Press". In: *New York*.

Tomanik, Eduardo et al. (2021). *Powertrain Friction Reduction by Synergistic Optimization of the Cylinder Bore Surface and Lubricant Part 1: Basic Modelling*. Tech. rep. SAE Technical Paper.

Thomas, TR and RS Sayles (1977). "Stiffness of machine tool joints: a random-process approach". In.

Ewins, David J (2009). *Modal testing: theory, practice and application*. John Wiley & Sons.

RESPONSIBILITY NOTICE

The authors are the only responsible for the printed material included in this paper.